10590 *Inorg. Chem.* **2010**, *49*, 10590–10597
DOI: 10.1021/ic101602a

Inorganic Chemistry
Article

Preparation and Bifunctional Gas Sensing Properties of Porous $In_2O_3-CeO_2$ Binary Oxide Nanotubes

Lin Xu, Hongwei Song,* Biao Dong, Yu Wang, Jiansheng Chen, and Xue Bai

State Key Laboratory on Integrated Optoelectronics, College of Electronic Science and Engineering, Jilin University, Changchun, 130012, People's Republic of China

Received August 8, 2010

The porous binary $In_2O_3-CeO_2$ oxides nanotubes (NTs) in cubic phase were first fabricated by electrospinning (ESP) method and characterized by SEM, TEM, XRD, XPS and UV−vis absorption techniques. By adjusting the In_2O_3 and CeO_2 molar ratio, the out diameters and wall thicknesses of the final composites were tuned ranging of 90−180 nm and 15−9 nm, respectively. The band gap of the binary oxides gradually decreases, and the ratio of Ce^{3+} to Ce^{4+} increases with the increase of CeO_2, implying that surface oxygen vacancies gradually increase. The gas sensing test reveals that when the content of CeO_2 is appropriate, the as fabricated $In_2O_3-CeO_2$ NTs could be bifunctional gas sensors to detect H_2S at low temperature(25−110 °C) while acetone at relative high temperature (300 °C). The $In_{75}Ce_{25}$ NTs sensor is an optimum one, which exhibits the highest response of 498 to H_2S at 80 °C and the highest response of 30 to acetone at 300 °C. In contrast to the pure In_2O_3 sensor, the response and recovery times, as well as the sensing reaction barrier height, for $In_{75}Ce_{25}$ both degrade considerably. The above temperature-dependent sensing properties were attributed to two different gas sensing mechanisms, sulfuration at low temperature and adsorption at high temperature.

Introduction

Significant interest has been generated during the past decade in the field of designing and preparing nanocomposites to explore the additional possibilities in developing novel materials. It is expected that they can not only exhibit enhanced properties, but also demonstrate diversified capabilities to be simultaneously exploitable in multiple applications. Among those nanocomposites, semiconductor-based binary oxides, such as $SnO_2-In_2O_3$, $TiO_2-In_2O_3$, In_2O_3-ZnO, and $Ga_2O_3-In_2O_3$, have gained extensive attention.[1] That is because of ongoing studies continued proving that in binary oxide system, because of strong interactions between the closely packed nanounits, its properties cannot be considered as a simple mixture of two individual components, but more complex and more superior in certain aspects.[1,2] Therefore, such structures have been used for a variety of applications, such as Li ion battery electrodes,[1a] photonics,[1b,c,2a] sensing,[1d] and even the bifunctional materials.[2d]

In_2O_3, as an important n-type III−VI semiconductor with a wide band gap of ~3.6 eV, exhibits promising properties in electronic and optical area.[3] In particular, In_2O_3 has been extensively applied in gas sensing, especially in detecting the toxic gases, such as, NH_3, H_2S, and NO_x.[4] Recent studies demonstrated that in the binary complexes, gas sensing properties of In_2O_3 could be improved greatly.[1d,5] Lin et al. fabricated the In_2O_3-ZnO films for NO_x gas sensing and found that suitable amount of ZnO adding into the In_2O_3 films could improve the corresponding response at low temperature.[1d] Chen et al. reported that through controlling the mixed ratio of In_2O_3 and SnO_2, the gas sensing performance to detect the toxic gas could be further enhanced.[5]

---

*To whom correspondence should be addressed. E-mail: hwsong2005@yahoo.com.cn. Tel./Fax: 86-431-85155129.

(1) (a) Kim, D. W.; Hwang, I. S.; Kwon, S. J.; Kang, H. Y.; Park, K. S.; Choi, Y. J.; Choi, K. J.; Park, J. G. *Nano Lett.* **2007**, *7*, 3041–3045. (b) Poznyak., S. K.; Talapin, D. V.; Kulak, A. I. *J. Phys. Chem. B* **2001**, *105*, 4816–4823. (c) Wang, N. W.; Yang, Y. H.; Yang, G. H. *J. Phys. Chem. C* **2009**, *113*, 15480–15483. (d) Lin, C. Y; Fang, Y. Y.; Lin, C. W.; Tunney, J. J.; Ho, K. C. *Sens. Actuators, B* **2010**, *146*, 28–34.

(2) (a) Xu, L.; Su, Y.; Li, S.; Chen, Y. Q.; Zhou, Q. T.; Yin, S.; Feng, Y. *J. Phys. Chem. B* **2007**, *111*, 760–766. (b) Agrawal, M.; Gupta, S.; Pich, A.; Zafeiropoulos, N. E.; Stamm, M. *Chem. Mater.* **2009**, *21*, 5343–5348. (c) Law, M.; Greene, L. E.; Radenovic, A.; Kuykendall, T.; Liphardt, J.; Yang, P. D. *J. Phys. Chem. B* **2006**, *110*, 22652–22663. (d) Chiu, W.; Khiew, P.; Cloke, M.; Isa, D.; Lim, H.; Tan, T.; Huang, N.; Radiman, S.; Abd-Shukor, R.; Abd. Hamid, M.; Chia, C. *J. Phys. Chem. C* **2010**, *114*, 8212–8218.

(3) (a) Li, C.; Zhang, D. H.; Han, S.; Liu, X. L.; Tang, T.; Zhou, C. W. *Adv. Mater.* **2003**, *15*, 143–146. (b) Yang, J.; Lin, C. K.; Wang, Z. L.; Lin, J. *Inorg. Chem.* **2006**, *45*, 8973–8979. (c) Zhang, Y.; Kolmakov, A.; Lilach, Y.; Moskovits, M. *J. Phys. Chem. B* **2005**, *109*, 1923–1929.

(4) (a) Li, C.; Zhang, D. H.; Liu, X. L.; Han, S.; Tang, T.; Han, J.; Zhou, C. W. *Appl. Phys. Lett.* **2003**, *82*, 1613–1615. (b) Kapse, V. D.; Ghosh, S. A.; Chaudhari, G. N.; Raghuwanshi, F. C. *Talanta* **2008**, *76*, 610–616. (c) Xu, P. C.; Cheng, Z. X.; Pan, Q. Y.; Xu, J, Q.; Xiang, Q.; Yu, W. J.; Chu, Y. L. *Sens. Actuators B* **2008**, *130*, 802–808.

(5) Chen, A. F.; Huang, X. D.; Tong, Z. F.; Bai, S. L.; Luo, R. X.; Liu, C. C. *Sens. Actuators B* **2006**, *115*, 316–321.

CeO_2 is a well-known rare earth oxide, which not only has peculiar characteristics arising from the 4f electronic shells[6] but also is a functional material compared to the other lanthanide.[7] In addition, the particular characteristics of CeO_2 make it a good candidate for gas sensing materials, such as its high oxygen storage capacity, which associates with its rich oxygen vacancies and low redox potential between Ce $^{3+}$ and Ce $^{4+}$.[8] Up to now, there are some works focused on the binary oxide containing CeO_2 as a component because of its unique properties. For example, $ZnO-CeO_2$, $MgO-CeO_2$, TiO_2-CeO_2, $CuO-CeO_2$, and $Fe_2O_3-CeO_2$.[9] However, to best of our knowledge, the synthesis of $In_2O_3-CeO_2$ binary oxides and their gas sensing properties have not been reported.

Various methods, such as thermal evaporation, coprecipitation, hydrothermal method, chemical vapor deposition, and sol-gel technique, have been put forward to synthesize the bicomposites materials.[1a,b,9] By comparison, ESP, a cost-effective and flexible platform for fiber spinning, offers several advantages, such as the extremely high surface-to-volume ratio because of the superlong scale in length, the porous substructure formed during annealing diameters and the controllable morphology by simply changing the electrospun parameters (the flow rate and the viscosity of solution).[10] Moreover, NTs structure can be obtained use this technique by adjusting the prepared process or improved electrospinning device. Here, in this paper, we present the first preparation of porous $In_2O_3-CeO_2$ NTs by one-step ESP method using PVP as the polymer and their bifunctional gas sensing characteristics based on different sensing mechanisms are also carefully studied.

Experimental Section

Preparation of $In_2O_3-CeO_2$ NTs. All chemicals used were analytical grade and without further purification. The $In_2O_3-CeO_2$ NTs were prepared by a novel and simple one-step electrospinning method as we used before.[11] In a typical synthesis, different molar ratios of $In(NO)_3 \cdot 4_{1/2}H_2O$ and $Ce(NO)_3 \cdot 6H_2O$ were dissolved into 10 mL of *N*,*N*-dimethylformamide (DMF) with magnetic stirring at room temperature. Through this paper, the mixed oxide samples are designed by the molar ratio of In to Ce and marked as $In_{75}Ce_{25}$, $In_{50}Ce_{50}$ and $In_{25}Ce_{75}$, corresponding to In/Ce molar ratios of 75:25, 50:50 and 25:75, respectively. After 30 min, appropriate amount of PVP were added into the mixed solutions to make the weight ratio of the inorganic to PVP equal to 0.36. Finally, colorless composite solutions were obtained after vigorous stirring for 3 h. Then, the composite solutions were loaded into the plastic syringes for ESP.

The precursor fibers were obtained by ESP with a collection distance of 15 cm between the spinneret tip and the collector and an applied steady-voltage of 16 kV under the protection of a N_2 stream. During the ESP, the solution jet solidified with accompanying evaporation of solvent and formed a nonwoven fibrous mat on the collector. After they were dried 12 h at room temperature under vacuum, the ESP fibers were annealed in a tube furnace with a rising rate of 1 °C/min from room temperature to 600 °C and maintained for 3 h; then, they were self-cooled down to room temperature again, forming the final NTs.

Characterization and Measurement. The surface morphology of the as-prepared samples was inspected using a JEOL JSM-7500F field emission scanning electron microscope (SEM) at an accelerating voltage of 15 kV with gold sputtered on samples. The average diameter of samples was calculated by selecting at least 100 fibers randomly from the SEM micrographs. The transmission electron microscopy (TEM) images were recorded on a JEM-2010 transmission electron microscope under a working voltage of 200 kV equipped with EDX spectrometer. X-ray diffraction (XRD) patterns of the samples were conducted on a Rigaku D/max 2550 X-ray diffractometer, using a monochromatized Cu target radiation resource (λ = 1.5045 Å). X-ray photoelectron spectroscopy (XPS) experiments were investigated using an ESCAlab 250 Analytical XPL Spectrometer with a monochromatic Al Kα source. All the binding energies were referenced to the C1s peak at 284.7 eV of the surface adventitious carbon. The fitted peaks in the XPS spectra were deconvoluted using the XPSPeak 4.1 software. The UV-vis-absorption spectra were measured on a Shimadzu 3600 UV-vis-NIR scanning spectrophotometer.

The gas sensing properties were measured on a WS-30A system (Weisheng Instruments Co. Zhengzhou, China). The $In_2O_3-CeO_2$ gas sensors were fabricated by coating the as-prepared NTs ethanol colloids on the ceramic tube (the coating thickness is about 0.25 mm) on which a pair of gold electrodes were previously printed. A small spring-like Ni-Cr alloy was inserted into the ceramic tube to provide the operating temperature. The gas sensors were dried and aged for 10 days before the first measurement. When testing, a given amount of target gases together with dry synthetic air were injected into the chamber (about 2.5 L in volume) to obtain desired concentrations. The response is defined as R_{air}/R_{gas}, where R_{air} and R_{gas} are the resistance for sensors in air and in target gas. The response and recovery times are defined as the time required reaching 80% of the final equilibrium value.

Results and Discussion

Characterization of $In_2O_3-CeO_2$ NTs. Figure 1 shows the typical SEM images of $In_{75}Ce_{25}$, $In_{50}Ce_{50}$, $In_{25}Ce_{75}$ and CeO_2 NTs, respectively. It could be observed that these randomly oriented NTs all had uniform and long continuous surface. The diameters of them are ~100, 120, 140, and 180 nm for $In_{75}Ce_{25}$, $In_{50}Ce_{50}$, $In_{25}Ce_{75}$ and CeO_2 NTs, respectively. Compared to the pure In_2O_3 NTs that we prepared before,[12] the diameters of them are gradually increased. In other words, the more the content of CeO_2 component is, the larger the diameter is. What is

---

(6) (a) Nyman, M.; Shea-Rohwer, L. E.; Martin, J. E.; Provencioa, P. *Chem. Mater.* **2009**, *21*, 1536–1542. (b) Tanner, P. A.; Mak, C. K.; Edelstein, N. M.; Murdoch, K. M.; Liu, G.; Huang, J.; Seijo, L.; Barandiarán, Z. *J. Am. Chem. Soc.* **2003**, *125*, 13225–13233. (c) Luwang, M.; Ningthoujam, R. S.; Jagannath; Srivastava, S. K.; Vatsa, R. K. *J. Am. Chem. Soc.* **2010**, *132*, 2759–2768.

(7) (a) Corma, A.; Domine, M. E. *Chem. Commun.* **2005**, *15*, 4042–4044. (b) Liao, L.; Mai, H. X.; Yuan, Q.; Lu, H. B.; Li, J. C.; Liu, C.; Yan, C. H.; Shen, Z. X.; Yu, T. *J. Phys. Chem. C* **2008**, *112*, 9061–9065. (c) Kumar, A.; Babu, S.; Karakoti, A. S.; Schulte, A.; Seal, S. *Langmuir* **2009**, *25*, 10998–11007.

(8) (a) Glaspell, G.; Fuoco, L.; El-Shall, M. S. *J. Phys. Chem. B* **2005**, *109*, 17350–17355. (b) Machida, M.; Uto, M.; Kurogi, D.; Kijima, T. *Chem. Mater.* **2000**, *12*, 3158–3164.

(9) (a) Ma, T. Y.; Yuan, Z. Y.; Cao, J. J. *Eur. J. Inor. Chem.* **2010**, *5*, 716–724. (b) Abimanyu, H.; Ahn, B. S.; Kim, C. S.; Yoo, K. S. *Ind. Eng. Chem. Res.* **2007**, *46*, 7936–7941. (c) Watanabe, S.; Ma, X. L.; Song, C. S. *J. Phys. Chem. C* **2009**, *113*, 14249–14257. (d) Tang, X. L.; Zhang, B. C.; Li, Y.; Xu, Y. D.; Xin, Q.; Shen, W. J. *Catal. Today* **2004**, *93–95*, 191–198. (e) Luo, M. F.; Ma, J. M.; Lu, J. Q.; Song, Y. P.; Wang, Y. J. *J. Catal.* **2007**, *246*, 52–59. (f) Bao, H. Z.; Chen, X.; Fang, J.; Jiang, Z. Q.; Huang, W. X. *Catal. Lett.* **2008**, *125*, 160–167.

(10) (a) Fridrikh, S. V.; Yu, J, H.; Brenner, M.; Rutledge, G. *Phys. Rev. Lett.* **2003**, *90*, 144502–144524. (b) Song, H. W.; Yu, H. Q.; Pan, G. H.; Bai, X.; Dong, B.; Zhang, X. T.; Hark, S. K. *Chem. Mater.* **2008**, *20*, 4762–4767.

(11) Xu, L.; Song, H. W.; Dong, B.; Wang, Y.; Bai, X.; Wang, G. L.; Liu, Q. *J. Phys. Chem. C* **2009**, *113*, 9609–9615.

(12) Xu, L.; Dong, B.; Wang, Y.; Bai, X.; Liu, Q.; Song, H. W. *Sensors Actuators B* **2010**, *147*, 531–538.

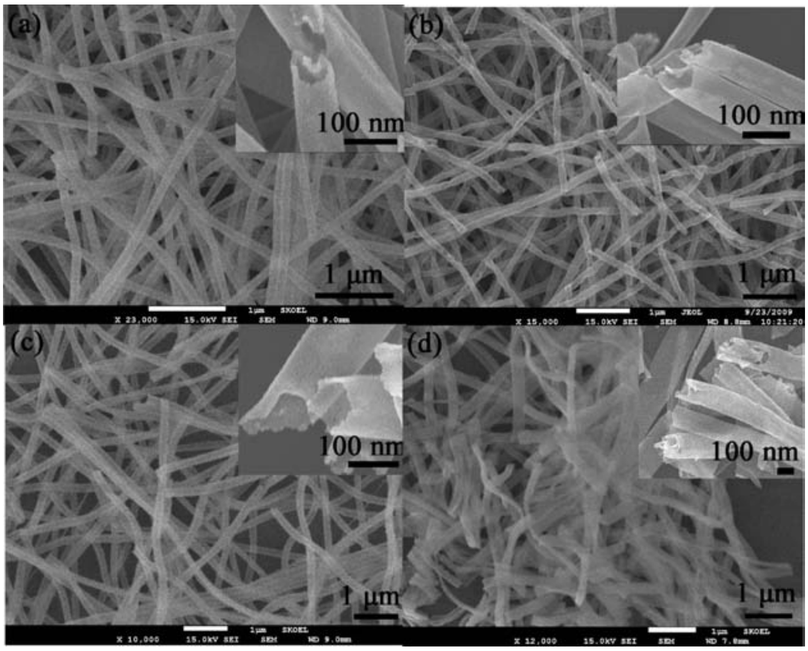

Figure 1. SEM images of (a) $In_{75}Ce_{25}$, (b) $In_{50}Ce_{50}$, (c) $In_{25}Ce_{75}$, and (d) CeO_2 nanotubes. The insets show the corresponding closeups of the nanotube sections.

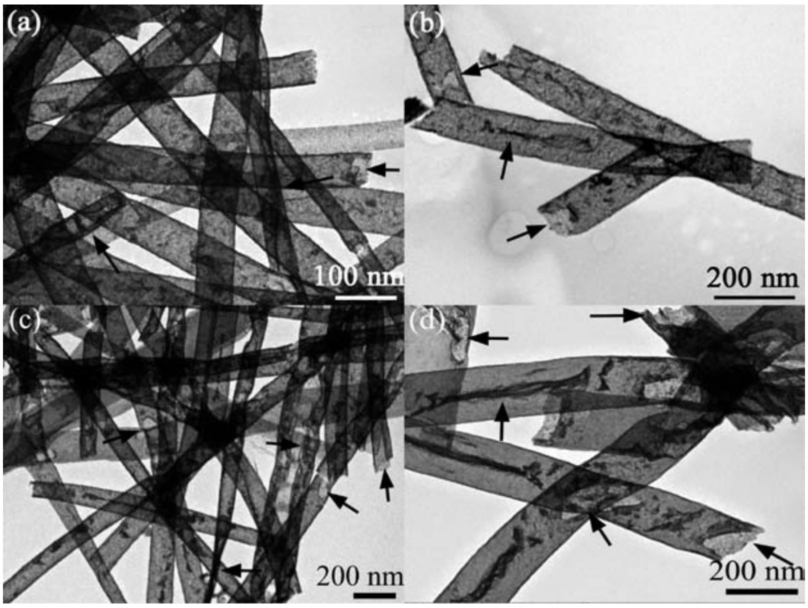

Figure 2. TEM images of (a) $In_{75}Ce_{25}$, (b) $In_{50}Ce_{50}$, (c) $In_{25}Ce_{75}$, and (d) CeO_2 nanotubes.

interesting, the wall thickness of the NTs shows a decreasing trend, ~ 12, 10, 9, and 9 nm for $In_{75}Ce_{25}$, $In_{50}Ce_{50}$, $In_{25}Ce_{75}$, and CeO_2 NTs, respectively (see inset of each panel of Figure 1), and the wall becomes soft and friable. It is suggested that the continuously decreasing wall thickness can not be fully supported by the whole nanotube and thus make the diameter in a certain direction increase. This phenomenon can be observed more clearly in TEM images.

To further confirm the morphologies of NTs, the TEM images are given in Figure 2. The samples show a porous structure agglomerated with very small particles. The arrows' direction in the TEM images are pointed to cross sections, folding parts, and broken parts of the NTs walls. As is shown, as the CeO_2 content increases, the diameter increases and the thickness of NTs wall gradually becomes thin, leading the NTs to become fragile after ultrasound. This situation was manifested by the increased number of the folding parts and the broken parts of the NTs walls.

According to our previous work, the formation mechanism of $In_2O_3-CeO_2$ NTs can be described as follows.[11] First, some In_2O_3 and CeO_2 primary nanoparticles were formed in the precursor fibers with the gradually removing of PVP in the annealing, which was controlled by the slowly heating rate. At a relatively lower temperature, the reaction rate on the outside was larger than that in the inner because of thermal unbalance,

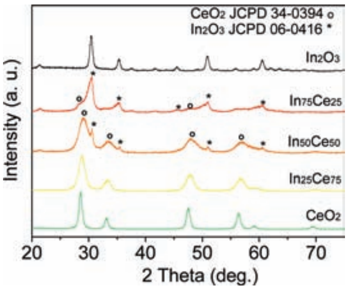

Figure 3. XRD patterns of pure In_2O_3, CeO_2, and $In_2O_3-CeO_2$ nanocomposites.

leading to the constriction of outside NPs and formation of loose nanowires. At an appropriate temperature (here is 600 °C), the reaction rate in the inner sites more quickly increased. In this case, the outside particles constricted, while the inner particles expanded because of the large strain strength, leading to the formation of NTs.

The XRD patterns for In_2O_3, CeO_2, and $In_2O_3-CeO_2$ nanocomposites are shown in Figure 3, which provide further insight into the crystallinity of the products. The XRD pattern taken from the pure In_2O_3 and CeO_2 NTs can be both indexed to cubic phase (JCPDS card 06-0416 for In_2O_3 and JCPDS card 34-0394 for CeO_2). For samples $In_{75}Ce_{25}$ and $In_{50}Ce_{50}$, there are no obvious peak shifts or any trace of other phases besides cubic In_2O_3 and CeO_2. Therefore, the crystal structure of samples $In_{75}Ce_{25}$ and $In_{50}Ce_{50}$ are considered to be mainly originated from the mixture of cubic In_2O_3 and CeO_2 with separate phases. The XRD patterns of $In_{25}Ce_{75}$ mixed oxide are similar to pure cubic CeO_2 but becoming broader. The same phenomenon was also observed in the other binary oxide contained CeO_2 when its content was dominant, such as MnO_x-CeO_2[13] and TiO_2-CeO_2[10c].

To further investigate valence chemistry and binding energy of constituent element of the as-prepared NTs samples, XPS spectra of different samples were studied, as shown in Figure 4. The survey spectra of all of the samples confirm the presence of In, O, Ce, and C (see Figure 4a). The peak at 284.7 eV is attributed to ethanol or CO_2 adsorbed on the surfaces of the NTs.[14] As is shown, when the content of different components changes in the composites, from $In_{75}Ce_{25}$ to $In_{25}Ce_{75}$, the intensity of the In_2O_3 and CeO_2 characteristic peaks also change in the same trend. Different from XRD analysis, both the In_2O_3 and CeO_2 peaks can be clearly observed in sample $In_{25}Ce_{75}$, further indicating that the sample consists of a mixture of In_2O_3 and CeO_2 with separate condition.

The O 1s XPS spectra of various samples are enlarged in Figure 4b. The XPS spectra of O1s core level electrons measured from In_2O_3 NTs display two peaks, with binding energies of 530.1 and 532.0 eV, corresponding to the lattice oxygen in crystalline In_2O_3[15] and chemisorbed oxygen and water related species,[16] respectively. Note that, in Figure 4b, the O 1s signals present shoulders located at the high binding energy (531.9−532.8 eV) side of each main peaks for every sample, which are all assigned to the OH species on the surface. The O 1s XPS spectrum of pure cubic CeO_2 can be well dissolved by two major components and a shoulder with O 1s binding energies, at 529.6, 530.2, and 532.8 eV, respectively. Praline et al. previously reported that oxygen coordinated to Ce^{3+} showed a higher binding energy than oxygen bound to Ce^{4+} in CeO_2.[17] Thus, peaks located at 529.6 and 530.2 eV can be unambiguously assigned to oxygen bound to Ce^{4+} and Ce^{3+}, respectively. Because the complicate chemical environments of O in mixed oxides, each characteristic peak has some shift. The corresponding binding energies and atomic ratio percentages for different characteristic peaks of O 1s in composite oxides are listed in Table 1. As shown in Table 1, the ratio of oxygen coordinated to Ce^{3+} increases gradually with the increase of CeO_2 content, suggesting more surface oxygen vacancies are formed. It is clear that the amount of the hydroxyl groups on the surface of the mixed oxides decrease greatly compared to the pure In_2O_3 and CeO_2.

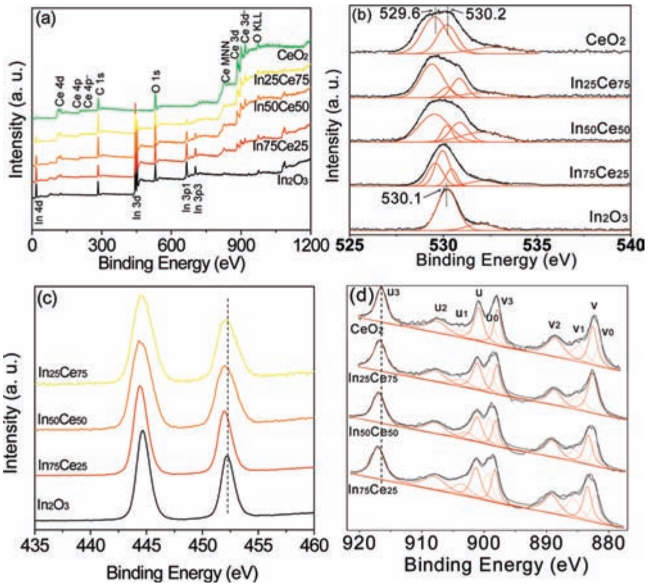

Figure 4. (a) Survey and (b) O 1s high resolution XPS spectra of pure In_2O_3, CeO_2, and $In_2O_3-CeO_2$ nanocomposites, (c) In 3d high resolution XPS spectra of pure In_2O_3 and $In_2O_3-CeO_2$ nanocomposites, and (d) Ce 3d high resolution XPS spectra of pure CeO_2 and $In_2O_3-CeO_2$ nanocomposites.

All four samples, as shown in Figure 4c show characteristic spin−orbit split for In $3d_{5/2}$ and In $3d_{3/2}$ of trivalent indium. The pure In_2O_3 shows In3d peaks assigned to In $3d_{5/2}$ and In $3d_{3/2}$ at 444.6 and 452.2 eV. In the case of $In_2O_3-CeO_2$ samples, all of the peaks of In3d of the $In_2O_3-CeO_2$ binary oxides shift to the low binding energy by ∼0.2 eV after the mixing of CeO_2. This can be explained by the charge density difference between metal ions.[18] The ion radiis of In^{3+}, Ce^{4+}, and Ce^{3+} are 81, 92, and 103.4 pm, respectively. The higher charge density ions of Ce can

---

(13) (a) Machida, M.; Uto, M.; Kurogi, D.; Kijima, T. *Chem. Mater.* **2000**, *12*, 3158–3164. (b) Qi, G.; Yang, R. T. *J. Phys. Chem. B* **2004**, *108*, 15738–15747.

(14) Zhang, Y. W.; Si, R.; Liao, C. S.; Yan, C. H. *J. Phys. Chem. B* **2003**, *107*, 10159–10167.

(15) Chen, C. L.; Chen, D. R.; Jiao, X. L.; Chen, S. H. *J. Phys. Chem. C* **2007**, *111*, 18039–18043.

(16) Erdem, B.; Hunsicker, R. A.; Simmons, G. W.; Sudol, E. D.; Dimonie, V. L.; El-Aasser, M. S. *Langmuir* **2001**, *17*, 2664–2669.

(17) Praline, G.; Koel, B. E.; Hance, R. L.; Lee, H. I.; White, J. M. *J. Electron Spectrosc. Relat. Phenom.* **1980**, *21*, 17–30.

(18) Na, C. W.; Bae, S. Y.; Park, J. *J. Phys. Chem. B* **2005**, *109*, 12785–12790.

Table 1. Corresponding Binding Energies (BE, eV) and Atomic Ratio Percentages (ARP, %) for Different Characteristic Peaks of O 1s in Composite Oxides

	O_{In}		O_{Ce}^{4+}		O_{ce}^{3+}		O_{OH}	
samples	BE	ARP	BE	ARP	BE	ARP	BE	ARP
In_2O_3	530.2	82.7					532.8	16.8
$In_{75}Ce_{25}$	530.0	42.9	529.6	29.1	530.4	15.4	532.1	12.7
$In_{50}Ce_{25}$	530.1	25.2	529.5	46.9	530.9	20.1	532.1	9.8
$In_{25}Ce_{75}$	530.1	15.2	529.4	51.0	530.8	20.5	532.8	9.8
CeO_2			529.5	54.6	530.2	32.2	532.8	17.3

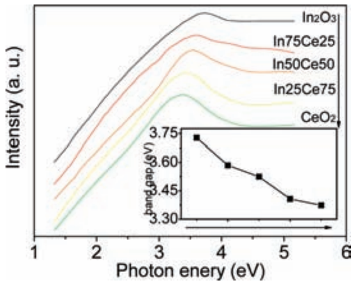

Figure 5. UV−vis absorption spectra of In_2O_3, $In_{75}Ce_{25}$, $In_{50}Ce_{50}$, $In_{25}Ce_{75}$, and CeO_2 and inset is the corresponding bang gaps of each sample.

withdraw the electrons from In, so the screening effect of electrons would decrease for In but increase for Ce (see Figure 4d). This implies that the incorporation of In/Ce can significantly influence the structure of valence band states.

Ce 3d electron core level XPS spectra seem more complex, which arises from the multiplicity of final states reached during the Ce 3d photoionization process.[19] As seen in Figure 4d, the 3d level can be dissolved into two series of peaks: The peaks labeled u are the result of the $3d_{3/2}$ spin−orbit states, and those labeled v are the corresponding $3d_{5/2}$ states. According to the corresponding deconvoluted peaks, six typical Ce3d binding energy peaks, labeled as v, v_2, v_3, u, u_2, and u_3, for every sample in Figure 5d are consistent with the previous report of Ce^{4+}.[20] In detail, the u/v and u_2/v_2 doublets are specific features resulting from the transfer of one or two electrons from a filled O 2p orbital to an empty Ce 4f orbital and u3/v3 doublet is due to the primary photoemission from $Ce^{4+}-O_2$.[21] The peaks marked by v_0, v_1, u_0, and u_1 are the characteristic peaks of Ce^{3+} and the u_1/v_1doublet is due to photoemission from Ce^{3+} cations.[19a] From the above analysis, we can conclude that the Ce 3d spectrum of the $In_2O_3-CeO_2$, as well as CeO_2 samples, basically denote a mixture of Ce^{3+}/Ce^{4+} oxidation states indicating that the surface of the sample is not fully oxidized and the Ce^{3+} ions are mainly located on the surface of the nanocrystals.[22] The surface atomic concentration of Ce^{3+} is determined to be 27.6, 25.4, 29.6, and 32.6% for $In_{75}Ce_{25}$, $In_{50}Ce_{50}$, $In_{25}Ce_{75}$, and CeO_2, respectively. It is worth mentioning that the relative Ce_2O_3 contents in the as-synthesized NTs by ESP are higher than those prepared by other methods, such as coprecipitation technique (14−23.5%).[23] This phenomenon can be explained by the reduced environment provided by the decomposition of PVP during the annealing, which might contain the carbon and hydrogen atmosphere and it tended to promote the formation of products with less oxygen (Ce_2O_3 in this case).[11]

Figure 5 shows the UV−vis absorption properties of the In_2O_3, CeO_2, and $In_2O_3-CeO_2$ nanocomposites NTs family. As is displayed, the absorption peak of In_2O_3 centers at 3.72 eV and band gap of CeO_2 located at 3.37 eV, both of which are higher than that of bulk In_2O_3 (3.67 eV) and CeO_2 (3.15 eV).[22,24] This phenomenon can be attributed to the large surface-to-volume ratio provided by tubular structure and porous nature, which induces a hydrostatic pressure because of the Gibbs−Thomson effect and the increase of band gap energy.[25] In addition, for CeO_2 NTs, the valence change from Ce^{4+} to Ce^{3+} on the surface of NTs, which had been proved by XPS, might have some additional contributions to the absorption of CeO_2 NTs. The change from +4 to +3 increases the direct charge-transfer gap between O 2p and Ce 4f bands, which leads to the shift of absorption spectrum of CeO_2 nanocrystals compared with bulk CeO_2.[26] The band gaps of the mixed oxide shift to low energy side gradually with an increase of the CeO_2 content, as shown inset of Figure 5. The regular shift of the band gaps of those binary oxides can be mainly assigned to the interfacial effects between In_2O_3 and CeO_2 grains.[9a]

Gas Sensing Properties of $In_2O_3-CeO_2$ NTs. As we know, H_2S is a highly toxic and flammable gas, which has been widely used in chemical industry, and it is also a mainly component in coal and natural gas. It is a dangerous gas for human bodies, even exposure at lower concentrations can result in adverse effect to the human health (when its concentration is greater than 250 ppm). Acetone gas sensors also exhibit significant application on the field of biomedical, chemical industries, and personal safety. Herein, gas sensing properties of the as-synthesized $In_2O_3-CeO_2$ NTs, as well as pure In_2O_3 and CeO_2 NTs, toward to H_2S and acetone are investigated.

The response of $In_2O_3-CeO_2$ NTs gas sensors to H_2S and acetone as a function of operating temperature is exhibited in Figure 6. It is well-known that the response of a semiconductor based gas sensor is highly affected by operating temperature. For H_2S gas detective, as can be observed in Figure 6, the mainly effective responses are concentrated in the lower temperature part. The response of $In_{75}Ce_{25}$ gas sensor is systemically higher than that of pure In_2O_3, while the response of $In_{50}Ce_{50}$ gas sensor shows a lower trend, and there is almost no response for $In_{25}Ce_{75}$ and pure CeO_2 gas sensors. Moreover, the optimal working temperature increases gradually when the content of CeO_2 increases. The optimal working temperature for pure In_2O_3 gas sensor is room temperature, corresponding to a response of 167. It is 80 °C for

---

(19) (a) Ho, C.; Yu, J. C.; Kwong, T.; Mak, A. C.; Lai, S. *Chem. Mater.* **2005**, *17*, 4514–4522. (b) Pfau, A.; Schierbaum, K. D. *Surf. Sci.* **1994**, *321*, 71–80.

(20) Force, C.; Román, E.; Guil, J. M.; Sanz, J. *Langmuir* **2007**, *23*, 4569–4574.

(21) Reddy, B. M.; Khan, A.; Yamada, Y.; Kobayashi, T.; Loridant, S.; Volta, J. C. *J. Phys. Chem. B* **2003**, *107*, 5162–5167.

(22) Wang, Z. L.; Quan, Z. W.; Lin, J. *Inorg. Chem.* **2007**, *46*, 5237–5242.

(23) Kumar, A.; Babu, S.; Karakoti, A. S.; Schulte, A.; Seal, S. *Langmuir* **2009**, *25*, 10998–11007.

(24) Zhu, H.; Wang, X. L.; Qian, L.; Yang, F.; Yang, X. R. *J. Phys. Chem. C* **2008**, *112*, 4486–4491.

(25) Xu, L.; Dong, B.; Wang, Y.; Bai, X.; Chen, J. S.; Liu, Q.; Song, H. W. *J. Phys. Chem. C* **2010**, *114*, 9089–9095.

(26) Tsunekawaa, S.; Fukuda, T. *J. Appl. Phys.* **2000**, *87*, 1318–1321.

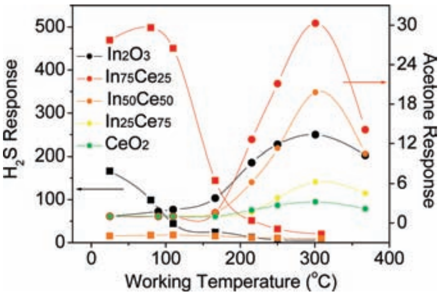

Figure 6. Response of NTs gas sensors to for 20 ppm H_2S and 200 ppm acetone as a function of operating temperature.

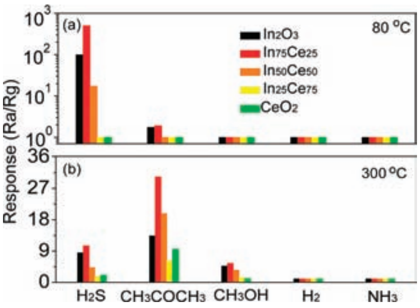

Figure 7. Selective test for (a) 20 ppm H_2S, H_2, NH_3, acetone, and methanol at 80 °C and (b) 200 ppm H_2S, H_2, NH_3, acetone, and methanol at 300 °C.

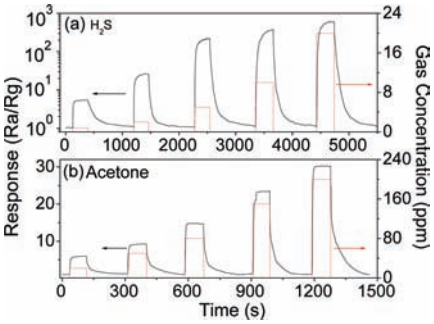

Figure 8. Dynamic response of $In_{75}Ce_{25}$ gas sensor to different H_2S concentrations (0.8−20 ppm) at 80 °C and acetone concentrations (10−200 ppm) at 300 °C.

$In_{75}Ce_{25}$ gas sensor, to a response of 498.6, and is 110 °C for $In_{50}Ce_{50}$ gas sensor, to a response of 17.8. Then, the responses all decrease quickly when the temperature further increases and when the temperature rises to 300 °C, all the response values decline to ~3. For acetone gas sensing, all the sensors have the same changing trend. The responses first increase with temperature, up to 300 °C, and then gradually decrease. All the maximum responses are at 300 °C, and the $In_{75}Ce_{25}$ gas sensor has largest response, ~30. Overall, this series of gas sensors have bifunctional sensing properties, which can be used as excellent H_2S gas sensors at relatively low operating temperature (room temperature to 110 °C), while good acetone gas sensors at relatively high temperature (300 °C). The $In_{75}Ce_{25}$ gas sensor is the best one, which has the optimum response both to H_2S and acetone.

To further confirm the versatility of the as-synthesized gas sensors, the selective test toward to H_2S, H_2, NH_3, acetone and methanol under 80 and 300 °C were conducted. Seen from Figure 7a, when the content of ceria is relative low ($In_{75}Ce_{25}$ and $In_{50}Ce_{50}$), the sensors show excellent selectivity to 20 ppm for H_2S at 80 °C while having almost no response to the other typical interference gases at the same temperature. This indicates that the present sensors have quite excellent selectivity to the H_2S assigned to their particular gas sensing mechanism, which will be discussed below. Figure 7b reveals that the gas sensors exhibit good sensitivity toward to acetone, compared to the other studied gases at 300 °C, and this further confirms the bifunctional ability of the low ceria contained gas sensors to detect both H_2S and acetone under different operating temperatures.

To obtain a deeper insight into the gas sensing behavior, attention was focused on $In_{75}Ce_{25}$ NTs, which is the most efficient in gas detection both to H_2S and acetone. Figure 8a shows the dynamic response of $In_{75}Ce_{25}$ NTs gas sensor exposed to different concentrations of H_2S around 80 °C. It is apparent that the responses of the sensor change rapidly as being exposed in air and in H_2S, indicating the excellent reproducible performance. The response time and recovery time are calculated to be 64 and 204 s, respectively. Figure 8b shows the switching response of $In_{75}Ce_{25}$ NTs gas sensor to different concentrations of acetone at 300 °C. The NTs gas sensor also shows a reversible yet stable response to acetone. The response and recovery times in acetone are determined for all the oxide sensors, they are 15 and 95s for In_2O_3, 9 and 80 s for $In_{75}Ce_{25}$, 8 and 54 s for $In_{50}Ce_{50}$, 8 and 49 s for $In_{25}Ce_{75}$, and 6 and 40 s for CeO_2, respectively. Obviously, the response and recovery times both decrease with the increase of CeO_2 content, which can be attributed to the increase of surface oxygen vacancies, as determined by XPS spectra.

Actually, the response and recovery time constants of $In_{75}Ce_{25}$ NTs gas sensor at various temperatures compared with the pure In_2O_3 are also measured, as shown in Figure 9 in the form of the logarithm of time constants versus the reverse of absolute temperature. It can be observed that the response and recovery time constants both increase with the decreasing temperature and have a turning point around 2.3×10^{-3} K^{-1} (160 °C). Using the well-known thermal activation function, the forward (ΔE_{res}) and backward reaction (ΔE_{rec}) barrier heights corresponded to response and recovery processes, respectively, can be fitted.[12] Accordingly, we fitted the data by two linear functions. The results reveal that ΔE_{res} values of $In_{75}Ce_{25}$ NTs gas sensor are 42 (25−160 °C, 1) and 134 meV (160−300 °C, 2), decreased twice compared to pure In_2O_3, the ΔE_{res} values of which are deduced to be 89 (25−160 °C, 3) and 279 meV (160−300 °C, 4). ΔE_{rec} values are fitted to be 110 (25−160 °C, 5) and 295 meV (160−300 °C, 6) for the $In_{75}Ce_{25}$ NTs related to 110 (25−160 °C, 7) and 380 meV (160−300 °C, 8) for the In_2O_3 NTs. It can be seen that at different temperature ranges the reaction barriers (ΔE_{res} and ΔE_{rec}) are quite different, suggesting that two different mechanisms exist at low temperature (25−160 °C) and high temperature ranges (160−300 °C).

Figure 10 shows the sensor response versus H_2S and acetone concentration. Figure 10a reveals the responses of H_2S in the range of 0.1−50 ppm at 80 °C. The $In_{75}Ce_{25}$ NTs sensor exhibit high response and the response is

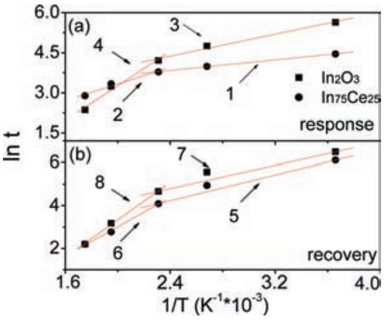

Figure 9. Logarithm of (a) the response time constant and (b) recovery time constants (both in second) of $In_{75}Ce_{25}$ NTs gas sensor compared to pure In_2O_3 versus the reverse of temperature. The dots are experimental data and the lines are the linear fitting functions.

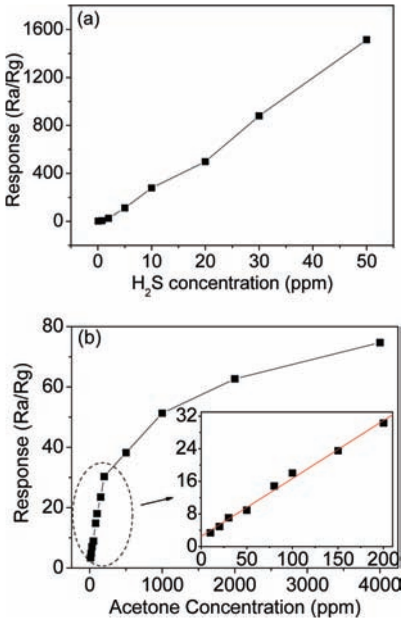

Figure 10. $In_{75}Ce_{25}$ gas sensor response curves to different H_2S concentrations (0.1−50 ppm) at 80 °C and acetone concentrations (10−4000 ppm) at 300 °C. The red line is the fit one.

positive proportional with the growth of the concentration. It should be mentioned that the fabricated sensor exhibits a clear and fast response of about 5.6 even for the very low H_2S concentration of 0.8 ppm. Moreover, it presents a response as high as 1515 when exposed to 50 ppm H_2S without showing any trend of saturation. As seen from Figure 9b, the response increases rapidly with increasing acetone concentration below 1000 ppm and the sensor shows a slow growth with further increasing the acetone concentration. The inset in Figure 10b shows the linear dependence curve in the range of 10−200 ppm, which further confirms the as-fabricated gas sensor can be used as a promising candidate for acetone detection.

For In_2O_3 and CeO_2, the well-known sensing mechanism is explained as the adsorption and desorption of the gas molecules on the surface of the sensing materials, which can cause the change in resistance in air and in target gas.[4b,5,7a] Relatively high optimal working temperature is one important property of this mechanism. Because at low temperature, only those target gas molecules which have high activity can participate in the adsorptive reaction and as the temperature increases, more and more gas molecules can reach the activation energy, so the response will also rise. While the temperature is too high, the desorption will become a dominant part compared to adsorption, so the response will decline. Generally, the working temperature of this mechanism is 250−500 °C or higher.[7b] For In_2O_3-based low-temperature H_2S gas sensing, a special sensing mechanism also plays an important role, which demonstrates as the sulfuration and desulfuration of the sensing materials.[12] As we have proved for H_2S detective, the surface adsorption and the sulfuration both contribute to the sensing response: at relatively low temperature range (25−160 °C), the sulfuration of In_2O_3 is the dominant mechanism, and at relatively high temperature range (160−300 °C), the surface adsorption is the main part.

Inspired by analysis of different gas sensing mechanisms, we reasonably proposed that both the adsorption and the sulfuration processes take contributions for detecting H_2S and acetone at different working temperatures. Taking $In_{75}Ce_{25}$ gas sensor for example, the $In_{75}Ce_{25}$ gas sensor has a very high response to 20 ppm H_2S (R_a/R_g = 498) at 80 °C, which is a low working temperature, whereas it only has a weak response ($R_a/R_g < 2$ to acetone) or no response ($R_a/R_g = 1$ to CH_3OH, H_2, and NH_3) to other gases. So, the surface sulfuration process of $In_{75}Ce_{25}$ is the dominant mechanism at 80 °C because there is no sulfuration process for the other gases except H_2S. When $In_{75}Ce_{25}$ gas sensor works at 300 °C, it has the highest response to acetone, while also has some response to other gases in different degrees, and it possesses of much faster response and recovery times compared to those under sulfuration process. As is well-known, the relatively weak anti-interference and the fast reaction rate are also the features of the adsorption mechanism and then we can ascribe the response to acetone at 300 °C to adsorption mechanism.

It should be figured out that sulfuration process does not occur on the CeO_2 because of the very low response when exposed to H_2S no matter at what working temperature. That is why by increasing the content of CeO_2, the optimal working temperatures for detecting H_2S of the binary oxide gradually increases, from 80 °C of $In_{75}Ce_{25}$ gas sensor to 110 °C of $In_{50}Ce_{50}$ gas sensor compared to room temperature of pure In_2O_3 gas sensor, while the response values gradually decrease relative to pure In_2O_3 gas sensor at 80 °C except for $In_{75}Ce_{25}$, which has a higher response. The possible reason that responsible for the enhanced gas sensing properties of the $In_{75}Ce_{25}$ NTs sensor at 80 °C for H_2S can be explained as followed: First, the air resistance of $In_{75}Ce_{25}$ NTs sensor is largely increased (~ 341 kΩ) in air because of the uniform introduction of CeO_2, which has a higher resistance (~ 986 kΩ) than In_2O_3 (~ 80 kΩ). Then, when exposed to H_2S, the relatively small resistance increment of $In_{75}Ce_{25}$ NTs sensor (~ 0.7 kΩ of $In_{75}Ce_{25}$ NTs sensor compared to ~0.5 kΩ of In_2O_3 NTs sensor) makes the final response (response = R_{air}/R_{gas}) increase.

For acetone gas detection, as studied, introduced appropriate amount of CeO_2 enables the improvement of sensitivity. The redox couple of Ce^{3+} and Ce^{4+} and the high capacity of oxygen storage can be responsible for the higher response of $In_{75}Ce_{25}$ and $In_{50}Ce_{50}$ NTs gas sensors compared to pure In_2O_3 gas sensor. The coexistence and variable valency of Ce^{3+} and Ce^{4+} on the surface of the synthesized materials provide plenty of additional oxygen vacancies and moreover, Ce^{4+} is a scavenger of electrons and easily traps the electrons,[9a] both of which can adsorb more oxygen molecules when exposed in air. The chemisorbed oxygen is very limited on the surface of pure In_2O_3, which results in a lower response. Furthermore, the Ce^{3+} and Ce^{4+} redox couple can further react with the acetone molecules adsorbed on the NTs materials. As mentioned before, the response of pure CeO_2 to the studied gas is much lower than the pure In_2O_3, so when the CeO_2 content further increases, the response will decrease. Therefore, the as-fabricated $In_{75}Ce_{25}$ and $In_{50}Ce_{50}$ NTs gas sensors reasonably exhibit better performance.

Conclusions

In summary, this work is devoted to synthesis of porous $In_2O_3-CeO_2$ NTs that, to the best of our knowledge, has no literature precedents, by using facile one-step electrospinning technique. The coupled $In_2O_3-CeO_2$ materials possess a cubic phase mixed by In_2O_3 and CeO_2. It is believed that both the diameters and wall thicknesses of NTs can be periodically modulated, in the range of 90−180 nm and 15−9 nm, respectively, because of the different mixing ratio of In_2O_3 and CeO_2. In addition, coexistence of Ce^{4+} and Ce^{3+} on the surface of the $In_2O_3-CeO_2$ NTs is observed which would further contribute to the gas sensing ability and a notable and gradual shift of the band gap relative to pure In_2O_3 and CeO_2 are also confirmed. A series of novel gas sensors based on these composite oxides to detect H_2S and acetone are fabricated and studied. The obtained results demonstrated that the different mixing ratio has great effect on the gas sensing behavior and among them, $In_{75}Ce_{25}$ gas sensor is the outstanding one. For the $In_{75}Ce_{25}$, the sensor exhibits high response to H_2S at low working temperature (80 °C) and also strong response to acetone at relative high working temperature (300 °C), moreover, the response of $In_{75}Ce_{25}$ sensor increases ∼3 times both for H_2S and acetone at different working temperature in comparison to the undoped In_2O_3 NTs sensor. The present work suggests that the $In_2O_3-CeO_2$ NTs possess multifunctional gas sensing properties and is very promising potential application in H_2S and acetone at different working temperatures.

Acknowledgment. The authors are thankful for the financial support of the High-Tech Research and Development Program of China (863) (Grant No. 2007AA03Z314), the National Science Fund for Distinguished Young Scholars of China (Grant No. 60925018), the National Natural Science Foundation of China (Grant Nos. 50772042, 10704073 and 20971051), the Project 20100128 Supported by Graduate Innovation Fund of Jilin University and the Frontier Science and Interdisciplinary Innovation Projects of Jilin University (Grant Nos. 421030951419)